

# Toward Unpaired Multi-modal Medical Image Segmentation via Learning Structured Semantic Consistency

Jie Yang<sup>a,b</sup>, Ruimao Zhang<sup>b\*</sup>, Chaoqun Wang<sup>b</sup>, Zhen Li<sup>b</sup>, Xiang Wan<sup>b</sup>, Lingyan Zhang<sup>a\*</sup>

<sup>a</sup> Department of Medical Imaging, Longgang Central Hospital of Shenzhen

<sup>b</sup> Shenzhen Research Institute of Big Data, The Chinese University of Hong Kong (Shenzhen)

## Abstract

*Integrating multi-modal data to improve medical image analysis has received great attention recently. However, due to the modal discrepancy, how to use a single model to process the data from multiple modalities is still an open issue. In this paper, we propose a novel scheme to achieve better pixel-level segmentation for unpaired multi-modal medical images. Different from previous methods which adopted both modality-specific and modality-shared modules to accommodate the appearance variance of different modalities while extracting the common semantic information, our method is based on a single Transformer with a carefully designed External Attention Module (EAM) to learn the structured semantic consistency (i.e. semantic class representations and their correlations) between modalities in the training phase. In practice, the above-mentioned structured semantic consistency across modalities can be progressively achieved by implementing the consistency regularization at the modality-level and image-level respectively. The proposed EAMs are adopted to learn the semantic consistency for different scale representations and can be discarded once the model is optimized. Therefore, during the testing phase, we only need to maintain one Transformer for all modal predictions, which nicely balances the model's ease of use and simplicity. To demonstrate the effectiveness of the proposed method, we conduct the experiments on two medical image segmentation scenarios: (1) cardiac structure segmentation, and (2) abdominal multi-organ segmentation. Extensive results show that the proposed method outperforms the state-of-the-art methods by a wide margin, and even achieves competitive performance with extremely limited training samples (e.g., 1 or 3 annotated CT or MRI images) for one specific modality.*

## 1. Introduction

For the assessment of specific diseases, different modalities of imaging, such as computed tomography (CT) and

magnetic resonance imaging (MRI), usually provide different information on tissue structure. In clinical practice, the data with different physical principles of imaging have always been used together [13] to obtain a more comprehensive view of specific organs in disease assessment and treatment planning [2]. On the other hand, although the data from different modalities have dramatic differences in appearance, some similar techniques are always required to aid in diagnosis, such as quantitative assessment via semantic segmentation on CT/MRI [9]. Previous research has primarily focused on developing powerful segmentation models [1, 10, 24, 33] for single modality segmentation, such as CT or MRI. Due to the domain shift of different modalities, these well-trained models on one specific modality frequently fail when being deployed to another modality for real-world clinical analysis [3]. In addition, the separate training scheme is unable to exploit the mutual information from multiple modalities, resulting in the sub-optimal accuracy for each modality.

In the literature, some recent studies [6, 16, 27] have been presented to address the aforementioned issue via joint representation learning from multi-modalities. They directly align the feature representation of corresponding pixels from different modalities during the training phase. However, such joint representation learning principally necessitates spatial alignment and co-registered sequences between different modalities, e.g., multi-sequence MRI (T1, T1c, T2, FLAIR). For the unpaired multi-modal data, e.g., CT and MRI, such a scheme is infeasible because of the spatial misalignment. Recently, Valindria *et al.* [25] proposed four kinds of dual-stream CNNs to alleviate the negative domain shift between unpaired CT and MRI, where assigning modalities with their specific feature extractors greatly affects the model's parameter efficiency and limits the model's ability to handle more modalities.

Despite significant efforts to pursue multi-modal medical image segmentation, mining the semantic associations (e.g., the representations of same tissue regions in CT and MRI) and aligning the feature representations from unpaired multi-modal data remain challenging due to the fol-

lowing issues. **First**, discovering how to fully explore the semantic associations of multiple modalities is critical but very difficult because there is no pixel-to-pixel correspondence in the unpaired input images in practice. **Second**, distinct physical principles of the underlying image acquisition lead to the large visual variance of multi-modal data, thus how to design neural network architecture to leverage mutual information to improve overall performance on each modality is critical for multi-modal learning but remains intractable nowadays [9]. **Third**, how to maintain reciprocal boosting of multiple modalities and even achieve better segmentation results in many practical situations with limited scarce annotated data for one specific modality has not been well investigated in the literature.

To address these three issues, in this paper, we propose a novel method for performing unpaired multi-modal medical image segmentation based on a single Transformer by learning the structured semantic consistency between modalities, *i.e.* the consistencies of semantic class representations and their correlations. Specifically, the unpaired multi-modal medical images, *e.g.*, CT and MRI, are firstly fed into a shared Transformer backbone to extract multi-scale feature representations. For each modality, we further introduce a set of modality-specific class embeddings, each of which indicates a global representation of one semantic class. It is updated during the training phase to learn the specific class representation across the entire dataset. In practice, these modality-specific class embeddings can be learnable and fed into an elaborate External Attention Module (EAM) to interact with the feature maps of the corresponding modal images. By doing this, the image-specific class embeddings and their correlations for a certain modal image can be further extracted. Furthermore, structured semantic consistency across modalities can be achieved gradually by implementing consistency regularizations at the modality-level and image-level respectively. During the testing phase, we discard all EAMs and only hold a single Transformer for predicting the segmentation results of various modalities.

We conduct extensive experiments on two popular medical image segmentation scenarios with 2D and 3D model configurations. Experimental results show that our method outperforms the state-of-the-art methods with a large margin, *i.e.* 3.3% and 2.5% improvements on the overall mean Dice for two tasks respectively. Moreover, we evaluate our method with the few-shot segmentation setting on cardiac sub-structure segmentation. The proposed method could still achieve competitive performance against state-of-the-art methods, demonstrating the effectiveness of such scheme to deal with scenarios where annotated data for one of the modalities is scarce.

In summary, the main contributions of this paper are as follows:

(1) We propose a novel method for accurately segment-

ing unpaired multi-modal medical images. In the test phase, it only relies on a single Transformer architecture and discards any modality-specific modules for multi-modal prediction.

(2) We introduce a plug-and-play External Attention Module to assist the model in discovering the semantic association and learn the structured semantic consistency (*i.e.* semantic class representations and their corresponding correlations) by using any unpaired multi-modal medical images.

(3) We evaluate our method on two different multi-class segmentation tasks with 2D and 3D configurations, showing the effectiveness of our method. Additional experiments conducted by using extremely limited training samples of a particular modality also highlight the great advantage of the proposed method in the case of limited annotations. Our code will be available at <https://github.com/YangJie18/LSSC>.

## 2. Related Work

### 2.1. Domain adaptation

In medical image analysis, severe domain shift has been a long-standing obstacle to knowledge transfer between unpaired modalities obtained by different physical principles of imaging. To address this problem, research works on domain adaptation of models either in a semi-supervised [34] or unsupervised [3, 11] manner, aiming to effectively improve cross-modality representation learning. In order to use data more effectively, transferring the knowledge that can promote each other between different modalities, some works also focus on full-supervised multi-modality learning. In [25], Valindria *et al.* discussed the effectiveness of various dual-stream architectures, demonstrating that the domain shift between two unpaired modalities limits mutual information sharing. Followed by this, Dou *et al.* [9] proposed a multi-modal learning approach by employing modality-specific internal normalization layers to compute respective statistics of each modality, and conduct cross-modality knowledge distilling to reduce the gap of prediction distributions between modalities. Our work is motivated by these studies. However, instead of carefully constructing multi-modal networks with different feature fusion strategies, we aim to design the external plug-and-play module to help a single model to establish the structured semantic consistency of different modalities, realizing multi-modal predictions.

### 2.2. Vision Transformer

Currently, the studies about vision Transformer [8] also achieve great progress in image analysis and understanding. It is a convolution-free network architecture, which directly employs the attention mechanism to capture the long-

range dependence of a sequence of non-overlapping image patches. Followed by ViT, Touvron *et al.* [22] proposed DeiT that introduced a distillation strategy for Transformer to help with ViT training. And many other ViT variants are also proposed [4, 18, 21, 28, 32] which achieve promising performance compared with its counterpart CNNs on various vision tasks, such as image classification and semantic segmentation. Among them, the recently proposed Swin-Transformer [18] adopts shifted windows mechanism to greatly improve the Transformer’s efficiency and ensure the Transformer’s flexibility of multi-scale modeling. Driven by the encouraging performance in semantic segmentation on natural images by Transformer, TransUNet [5] firstly attempted to apply transformer to improve the segmentation performance of medical image, which adopts the CNN architecture to obtain a feature map as the input of Transformer. Inspired by TransUNet, Cao *et al.* [1] proposed a pure U-shaped transformer named Swin-UNet, where the architecture utilizes SwinTransformer block as the basic unit to improve its capacity of feature representation for 2D medical image segmentation. To explore Transformer’s ability to learn volumetric representations from 3D medical volumes, Zhou *et al.* [33] proposed nnFormer to interleave convolution and self-attention for medical volumetric segmentation, achieving tremendous progress over previous transformer-based medical segmentation methods.

Despite the apparent success of the Transformer in medical image segmentation, to best our knowledge, these Transformer-based methods are dedicated to exploring knowledge from one modality and perform poorly when transferred to test against other modalities. In addition, the use of attention mechanisms to learn to reduce modality discrepancy has not been well discussed in the literature. In this paper, we focus on uncovering the intrinsic benefits of a single Transformer in terms of modal reciprocity and evaluate its advantages over existing approaches.

### 3. Methodology

#### 3.1. Problem Setting and Framework Overview

Considering two unpaired medical images  $\{\mathbf{X}_{M_1}, \mathbf{X}_{M_2}\}$  extracted from different modalities and their corresponding label maps  $\{\mathbf{Y}_{M_1}, \mathbf{Y}_{M_2}\}$ , the proposed multi-modal learning framework aims to explore structured semantic information that bridge the modality gap at the training process and to produce a unified segmentation model for multiple modalities’ predictions, outperforming the one trained with a single modality.

The overall framework of the proposed method is depicted in Fig. 1. For simplicity, we use the 2D model as an illustration which can be easily extended to the 3D model. We first feed three consecutive slices as the inputs  $\{\mathbf{X}_{M_1}, \mathbf{X}_{M_2}\} \in \mathbb{R}^{3 \times H \times W}$  into the modality-specific im-

age embedding module, which is simply implemented by two consecutive  $1 \times 1$  convolutional layers, making the resolution and dimension of the inputs unchanged. The embedded feature maps from the two modalities are then fed into a single Transformer-based segmentation network that includes encoder and decoder subnetworks. Specifically, two embedded feature maps are divided into non-overlapping patch tokens with the size of  $P \times P$  before being fed into the hierarchical Transformer encoder. In this way, we could re-assign the dimension of the inputs as  $\{\mathbf{X}_{M_1}, \mathbf{X}_{M_2}\} \in \mathbb{R}^{3P^2 \times \frac{H}{P} \times \frac{W}{P}}$ . As shown in Fig. 1, both of the encoder and decoder contain 4 stages to generate the multi-scale representations, and the basic number of Transformer blocks are  $G_\lambda$  and  $L_\lambda$  for the encoder and decoder respectively, where  $\lambda \in \{1, 2, 3, 4\}$ . **For the encoder**, the patch embedding module at the Stage 1 converts the dimension of input tokens into  $C \times \frac{H}{P} \times \frac{W}{P}$ , where  $C$  denotes the feature dimension. The down-sampling modules in the other three stages are responsible for reducing the number of tokens by a quarter and doubling the dimension of tokens, generating multi-scale patch token representations, *i.e.*  $2C \times \frac{H}{2P} \times \frac{W}{2P}$  at Stage 2,  $4C \times \frac{H}{4P} \times \frac{W}{4P}$  Stage 3, and  $8C \times \frac{H}{8P} \times \frac{W}{8P}$  at Stage 4. **For the decoder**, the up-sampling modules are adopted to restore higher resolutions stage by stage, which in turn are fused with multi-scale representations from the corresponding encoder stages via skip connections. At last, the model predicts the pixel-wise class labels of two modalities’ images by using a single dense prediction layer. Please refer to Sec. 3.2 for more details about the Transformer Block design.

To align the modalities during training phase, we explore two kinds of semantic information, termed *modality-specific class embeddings* and *image-specific semantic correlations*. The former is a set of learnable vectors for each modality, each of which presents one semantic class, *e.g.*, Liver or Spleen. It aims to learn the global class representations of each modality. The latter is used to present the inter-class relationships within a specific image. In practice, a newly designed *External Attention Module* (EAM) is introduced to update the above learnable class embeddings from modality-specific to image-specific, and extract the semantic correlations of a specific image at multiple scales. As shown in Fig. 1, modality-specific class embeddings of a specific modality are denoted as matrix form  $\mathbf{Q} \in \mathbb{R}^{Z \times 4C}$ , where  $Z$  indicates the total number of classes and is consistent over different modalities. For simplicity, we do not distinguish  $\mathbf{Q}$  for different modalities. Thus, in this case, the  $\mathbf{Q}$  can correspond to the yellow hexagons for CT or the green hexagons for MRI in Fig. 1. We feed  $\mathbf{Q}$  into EAM to conduct interaction with the feature maps of the specific image at Scale-1, obtaining image-specific class embeddings  $\mathbf{Q}_1 \in \mathbb{R}^{Z \times 2C}$  and semantic correlations  $\mathbf{E}_1 \in \mathbb{R}^{Z \times Z}$ . To process the multi-scale feature maps,  $\mathbf{Q}_\lambda$  is then

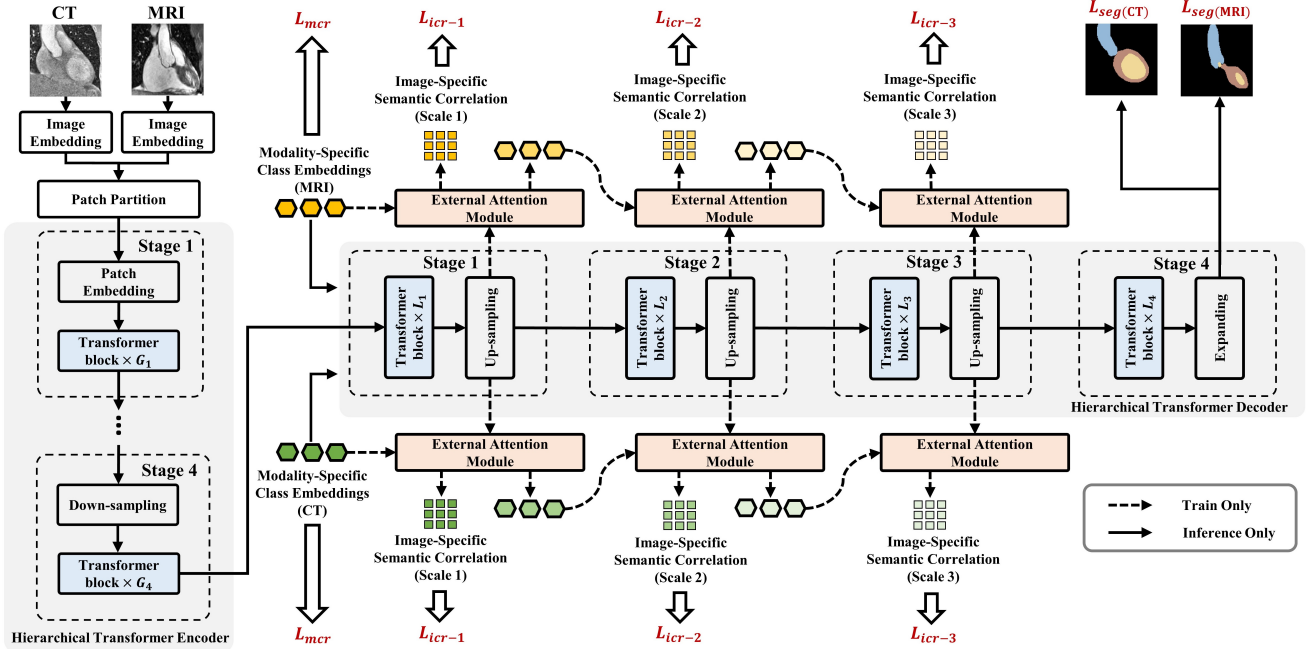


Figure 1. Overview of our proposed unpaired multi-modal medical image segmentation framework via single Transformer architecture and the proposed EAMs. Two unpaired medical images from different modalities are fed into the shared Transformer Encoder and Decoder for feature extraction and dense prediction. The *modality-specific class embeddings* for different modalities are introduced to learn modality-specific class representations, while fed into Transformer blocks for realizing the calibration of modality-specific activation (optional operation). The newly proposed External Attention Module (EAM) aims to conduct interaction between image features and modality-specific class embeddings, generating *image-specific semantic correlations*. To facilitate the consistency of the two modalities’ representations, the modality-specific class embeddings and image-specific semantic correlations are both aligned between the two modalities at the modality-level and image-level, respectively. Note that all parts linked by dotted lines can be removed during the inference phase.

passed into the EAM at Scale- $(\lambda + 1)$  to obtain  $\mathbf{Q}_{\lambda+1}$  and  $\mathbf{E}_{\lambda+1}$ , where  $\mathbf{Q}_{\lambda}$  is adapted to reflect class representations of a specific image within modality, and  $\mathbf{E}_{\lambda}$  presents the image-specific semantic correlations at Scale- $\lambda$ . In general,  $\mathbf{Q}_{\lambda} \in \mathbb{R}^{Z \times \frac{2C}{\lambda}}$ ,  $\lambda \in \{1, 2\}$  and  $\mathbf{E}_{\lambda} \in \mathbb{R}^{Z \times Z}$ ,  $\lambda \in \{1, 2, 3\}$ . We will provide a more detailed description of the operations in EAM in Sec. 3.3.

During the training phase, we explicitly facilitate the consistency of two modalities’ representations. 1) We firstly introduce the global consistency regularization  $\mathcal{L}_{mcr}$  to minimize the representation distance between modality-specific class embeddings. It aims to globally align the semantic class representations of two modalities. Such consistency will also implicitly affect the pixel-level representation learning of each sample, since these modality-specific class embeddings also interact with corresponding images of each modality through training process. 2) We further align semantic correlations between two modalities at image-level by minimizing  $\mathcal{L}_{icer}$ , which calculates symmetrical Kullback-Leibler divergence of any two images from different modalities. Such a scheme allows generating

many sample pairs to drive semantic correlation alignment, which makes the optimized model more robust to sample variation. 3) The alignment of image-specific semantic correlations at multiple stages can also overcome the effect of the scales and sizes of the semantic area of different modalities’ data. Please refer to Sec. 3.4 for more details about the objective function design.

### 3.2. Transformer Block

Following Vision Transformer [26], the Transformer Block includes the basic multi-head attention, layer normalization, and feed forward layer, as shown in Fig. 2-(a). Motivated by the LayerScale [23], we additionally introduce modality-aware channel-wise multiplication on the output of each residual operation in the Transformer block, with the goal of calibrating modality-specific activation in the channel dimension to assist the model in narrowing the discrepancy between representations from different modalities.

Given the modality-specific class embeddings  $\mathbf{Q} \in \mathbb{R}^{Z \times 4C}$  of a certain modality, where  $Z$  is the total number of classes and is constant across all modalities, and  $4C$



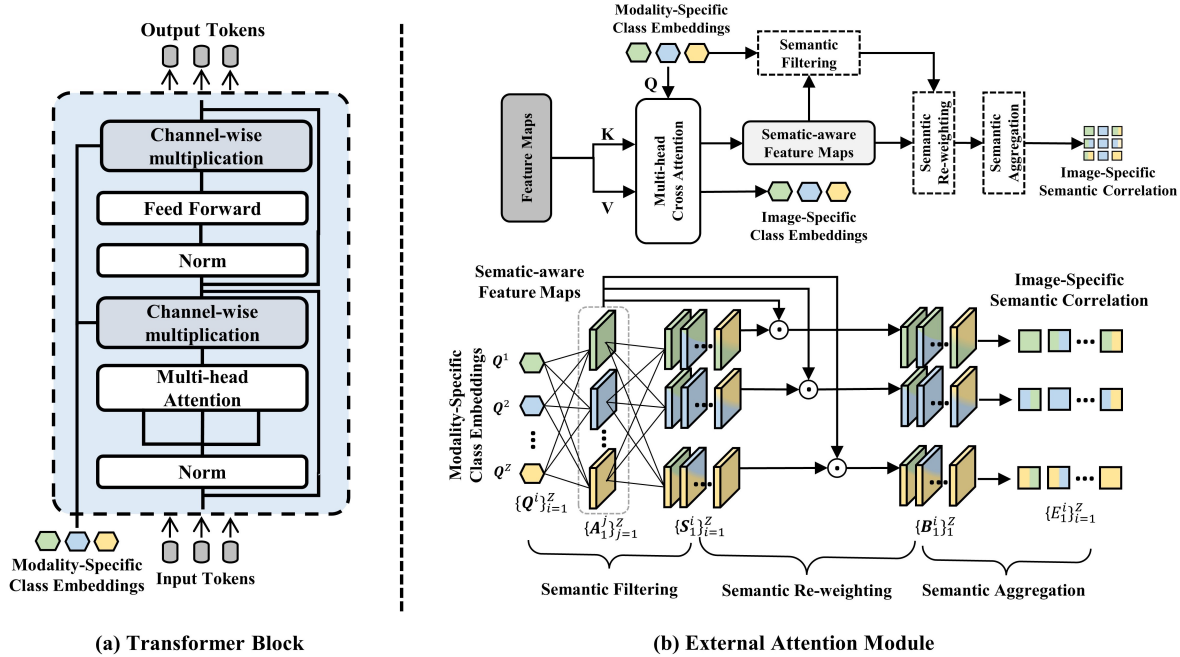


Figure 2. Illustration of (a) Transformer block with modality-specific channel-wise multiplication to calibrate the token feature representations. (b) External Attention Module (EAM) for the Stage-1 of Transformer Decoder, which adopts *modality-specific class embeddings* and feature maps at scale-1 as the input. In practice, we replace *modality-specific class embeddings* with *image-specific class embeddings* for Stage-2 and Stage-3, which is illustrated in Fig. 1. At the top of (b), modality-specific class embeddings first interact with feature maps via Multi-head Cross Attention to obtain image-specific class embeddings and semantic-aware feature maps at scale-1. Then, modality-specific class embeddings interact with semantic-aware feature maps via three-step processing to obtain image-specific semantic correlations. At the bottom of (b), we illustrate the detailed three-step process, *i.e.* semantic filtering, semantic re-weighting, and semantic aggregation, where the elements inside the dotted box denotes the semantic-aware feature maps  $\mathbf{A}_1$  presented in Sec. 3.3.

denotes the channel dimension, we aggregate its semantic information by using linear projection to produce modality-specific channel weight  $\Omega \in \mathbb{R}^{4C}$ . We then project  $\Omega$  to the corresponding feature dimensions (*e.g.*, from  $4C$  to  $D$  for the specific scale), and the  $\text{diag}(\cdot)$  operation is adopted to generate diagonal matrix to calibrate modality-specific activation as follows:

$$\begin{aligned} \Omega &= \mathbf{w}_1 \mathbf{Q}, \Phi_1 = \text{diag}(\Omega \mathbf{W}_2), \Phi_2 = \text{diag}(\Omega \mathbf{W}_3), \quad (1) \\ \mathbf{X}'_l &= \mathbf{X}_l + \Phi_1 \otimes \text{MSA}(\text{Norm}(\mathbf{X}_l)), \quad (2) \\ \mathbf{X}_{l+1} &= \mathbf{X}'_l + \Phi_2 \otimes \text{FFN}(\text{Norm}(\mathbf{X}'_l)), \quad (3) \end{aligned}$$

where  $\mathbf{w}_1 \in \mathbb{R}^Z$ ,  $\mathbf{W}_2 \in \mathbb{R}^{4C \times D}$ ,  $\mathbf{W}_3 \in \mathbb{R}^{4C \times D}$ ,  $\text{MSA}(\cdot)$  and  $\text{FFN}(\cdot)$  denote the multi-head attention layer and the feed forward layer respectively.  $\text{Norm}(\cdot)$  indicates the LayerNorm operation, and  $\otimes$  is the channel-wise multiplication.  $\mathbf{X}_l$  and  $\mathbf{X}_{l+1}$  denote the input and output of  $(l+1)$ -th transformer block.

As shown in Fig. 1, we feed the modality-specific class embeddings into Transformer decoder. In practice, we find that the modality-specific channel-wise multiplication can also calibrate the universal representations extracted in the Transformer encoder. Thus, we implement the above scheme in all Transformer blocks to improve accuracy even

further. It should also be noted that such modality-specific channel-wise recalibration is optional. If we need to remove the modality-specific class embeddings during inference, we could skip this scheme and instead use the original Transformer blocks proposed in [1, 33].

### 3.3. External Attention Module

In addition to defining the learnable modality-specific class embeddings to capture the class representations from different modalities, we also propose the External Attention Module (EAM) to conduct the interaction between these modality-specific embeddings and image features to generate class representation of each image, and derive semantic correlations of a certain modal image at multiple scales for further semantic alignment. For simplicity, we illustrate the proposed EAM using feature maps  $\mathbf{F} \in \mathbb{R}^{\frac{H}{4P} \times \frac{W}{4P} \times 4C}$  at Scale-1 in Fig. 2-(b), and such mechanism can be applied to other scales as well.

**Class Embeddings.** In practice, the learnable modality-specific class embeddings are used to learn the class representations of a specific modality across the entire dataset, while each image should have its own class representations that differ from the global ones due to their appearance variance. Thus, we employ the Cross-Attention Mech-

anism (CA) for updating class embeddings by interacting with multi-scale feature maps of a certain image to generate its image-specific class embeddings. Specifically, we utilize  $\mathbf{F} \in \mathbb{R}^{\frac{H}{4P} \times \frac{W}{4P} \times 4C}$  to calculate the key and value of CA by linear projection, while the query of CA is calculated employing modality-specific class embeddings  $\mathbf{Q} \in \mathbb{R}^{Z \times 4C}$  as follows:

$$\mathbf{q} = \mathbf{Q}\mathbf{W}_Q, \mathbf{k} = \mathbf{F}\mathbf{W}_K, \mathbf{v} = \mathbf{F}\mathbf{W}_V, \quad (4)$$

$$\text{CA}(\mathbf{Q}, \mathbf{F}) = \text{softmax}\left(\frac{\mathbf{q}\mathbf{k}^\top}{\sqrt{d}}\right)\mathbf{v}, \quad (5)$$

where  $\mathbf{W}_K, \mathbf{W}_V, \mathbf{W}_Q \in \mathbb{R}^{4C \times 4C'}$  are the parameter matrices for linear projection.  $d$  is the channel dimension of  $\mathbf{q} \in \mathbb{R}^{Z \times 4C'}$  and  $\mathbf{k} \in \mathbb{R}^{(\frac{H}{4P} \times \frac{W}{4P}) \times 4C'}$ . The  $\text{softmax}(\cdot)$  denotes the  $\text{softmax}$  function along the spatial dimension, i.e.  $\frac{H}{4P} \times \frac{W}{4P}$ . The  $\mathbf{q}\mathbf{k}^\top \in \mathbb{R}^{Z \times \frac{H}{4P} \times \frac{W}{4P}}$  indicates the *Semantic-aware Feature Maps* extracted from a single CA head at Scale-1, where  $Z$  denotes the total numbers of semantic classes. The Multi-head Cross Attention (MCA) is the extension with  $N$  independent CA operations and project their concatenated outputs as follows:

$$\text{MCA}(\mathbf{Q}, \mathbf{F}) = \mathbb{C}(\text{CA}_1(\mathbf{Q}, \mathbf{F}), \dots, \text{CA}_N(\mathbf{Q}, \mathbf{F}))\mathbf{W}_O, \quad (6)$$

where  $\mathbb{C}$  denotes the concatenation operation.  $\mathbf{W}_O \in \mathbb{R}^{4C' \times 4C}$  is the learnable parameter matrix, and we have  $4C' = 4C/N$ . In such multi-head setting, the *Semantic-aware Feature Maps* extracted from multiple attention heads at Scale-1 can be presented as  $\mathbf{A}_1 \in \mathbb{R}^{Z \times N \times \frac{H}{4P} \times \frac{W}{4P}}$ , which can be further adopted to derive image-specific semantic correlations in Fig. 2-(b). In this way, the  $\mathbf{Q}$  can be updated by:

$$\hat{\mathbf{Q}} = \text{MCA}(\text{Norm}(\mathbf{Q}), \text{Norm}(\mathbf{F})) + \mathbf{Q}, \quad (7)$$

$$\tilde{\mathbf{Q}} = \text{MLP}(\text{Norm}(\hat{\mathbf{Q}})) + \hat{\mathbf{Q}}, \quad (8)$$

where the operation  $\text{MLP}(\cdot)$  is the abbreviation for Multi-layer Perceptron, and  $\tilde{\mathbf{Q}} \in \mathbb{R}^{Z \times 4C}$  reflects image-specific class representations by collecting image-specific semantic information from feature maps of a particular modal image. In practice, the  $1 \times 1$  convolution operation is further used to reduce the dimension of the above  $\tilde{\mathbf{Q}}$  to  $Z \times 2C$  and obtain image-specific class embeddings  $\mathbf{Q}_1$  in Sec. 3.1 for the next scale of updates. The operations at the other scales are identical to those described above, and the only difference is that we adopt image-specific class embeddings (e.g.  $\mathbf{Q}_1$  or  $\mathbf{Q}_2$ ) to replace  $\mathbf{Q}$  in the above equations.

**Semantic Correlations.** The semantic correlations reflect the inter-class representation similarities. In practice, we propose a three-step processing to extract semantic correlation matrix in a specific image. Again, we explain the corresponding operations at Scale-1 as an illustration. As

shown in Fig. 2-(b), given the modality-specific class embeddings  $\mathbf{Q}$  and multi-head semantic-aware feature maps  $\mathbf{A}_1$ , the semantic correlations  $\mathbf{E}_1$  can be calculated via semantic filtering, semantic re-weighting and semantic aggregation, respectively. The operations at the other scales are the same, the only difference is that we replace  $\mathbf{Q}$  with image-specific class embeddings  $\mathbf{Q}_1$  and  $\mathbf{Q}_2$  to calculate  $\mathbf{E}_2$  and  $\mathbf{E}_3$ .

1) *Semantic Filtering.* Given a particular semantic class embeddings in  $\mathbf{Q}$ , the purpose of such a step is to calculate its relevance to all semantic classes at the token level. Since  $\mathbf{A}_1 \in \mathbb{R}^{Z \times N \times (\frac{H}{4P} \times \frac{W}{4P})}$ , the feature dimension of each token is  $Z \times N$ . We can further divide the features of tokens into  $Z$  groups, each of which is corresponding to a particular semantic class. Thus we have  $\mathbf{A}_1 = \{\mathbf{A}_1^j\}_{j=1}^Z$  and  $\mathbf{A}_1^j \in \mathbb{R}^{N \times \frac{H}{4P} \times \frac{W}{4P}}$ . Similarly, we can rewrite  $\mathbf{Q}$  as  $\{\mathbf{Q}^i\}_{i=1}^Z$  and  $\mathbf{Q}^i \in \mathbb{R}^{4C}$ . For  $i$ -th class, we first generate the semantic kernel as  $\mathbf{K}^i = \mathbf{Q}^i\mathbf{W}^i$ , where  $\mathbf{W}^i \in \mathbb{R}^{4C \times N}$  is the parameter matrix that is corresponding to the  $i$ -th class. To calculate the similarity between  $i$ -th and  $j$ -th classes at token level, we can directly reshape  $\mathbf{K}^i$  into  $\mathbb{R}^{N \times 1 \times 1}$  to perform filtering on  $\mathbf{A}_1^j$  as follows,

$$\mathbf{S}_1^{ij} = \mathbb{F}(\mathbf{K}^i, \mathbf{A}_1^j), \quad (9)$$

where the function  $\mathbb{F}(\cdot, \cdot)$  denotes the convolutional operation, and  $\mathbf{S}_1^{ij} \in \mathbb{R}^{\frac{H}{4P} \times \frac{W}{4P}}$  is a similarity map of  $i$ -th class for the  $j$ -th class, where tokens with higher response scores indicate the higher correlation to  $i$ -th class representation in  $\mathbf{Q}$ . That is reasonable in practice. Taking the multi-organ image of the abdomen as an example, intuitively, the left kidneys and right kidneys should have similar structural representations due to their similar appearance, shape and size. There usually exists a higher probability of inter-class similarity than in other organs. Thus, the class filter of left kidneys should have the highest response to the region of the left kidneys, followed by the second-highest response to the region of the right kidneys and a lower response to the other organs.

2) *Semantic Re-weighting.* Given similarity maps between  $i$ -th class representation in  $\mathbf{Q}$  and all groups' feature maps of  $\mathbf{A}_1$ , then we have  $\mathbf{S}_1^i = \{\mathbf{S}_1^{i1}, \dots, \mathbf{S}_1^{ij}, \dots, \mathbf{S}_1^{iZ}\} \in \mathbb{R}^{Z \times (\frac{H}{4P} \times \frac{W}{4P})}$ . By conducting the  $\text{softmax}$  operation on each spatial position of  $\mathbf{S}_1^i$ , each element in  $\mathbf{A}_1$  is weighted by the gating function as follows,

$$\mathbf{B}_1^i = \mathbf{A}_1 \odot \mathbb{B}(\sigma(\mathbf{S}_1^i)), \quad (10)$$

where  $\sigma(\cdot)$  is  $\text{softmax}$  operation,  $\mathbb{B}$  is the broadcast operation to extent the dimension of input to  $Z \times N \times \frac{H}{4P} \times \frac{W}{4P}$ , and  $\odot$  denotes the element-wise multiplication. In this way, we obtain  $\mathbf{B}_1^i = \{\mathbf{B}_1^{i1}, \dots, \mathbf{B}_1^{ij}, \dots, \mathbf{B}_1^{iZ}\} \in \mathbb{R}^{Z \times N \times (\frac{H}{4P} \times \frac{W}{4P})}$ , where  $\mathbf{B}_1^{ij}$  denotes the correlation map

between  $i$ -th class representation in  $\mathbf{Q}$  and  $j$ -th class feature maps.

3) *Semantic Aggregation.* To generate the final correlation map, we conduct the normalized summation on  $\mathbf{B}_1^i$  along the last three dimension to realize semantic aggregation,

$$\mathbf{E}_1^i = \frac{\sum_{(N, \frac{H}{4P}, \frac{W}{4P})} \mathbf{B}_1^i}{\sum_{(\frac{H}{4P}, \frac{W}{4P})} \sigma(\mathbf{S}_1^i)} \quad (11)$$

where  $\mathbf{E}_1^i \in \mathbb{R}^Z$  is the normalized correlation vector, and each element in  $\mathbf{E}_1^i$  presents the relevance between the  $i$ -th class representation in  $\mathbf{Q}$  and one specific class representation of the input image. Finally, image-specific semantic correlations at Scale-1 can be presented as  $\mathbf{E}_1 = \{\mathbf{E}_1^1, \dots, \mathbf{E}_1^i, \dots, \mathbf{E}_1^Z\} \in \mathbb{R}^{Z \times Z}$ . The operations of EAM at other scales are the same as Scale-1's, but with different input feature dimensions. It is worth noting that since there is no spatial alignment between two cross-modal images (e.g. CT and MRI), there may have a huge difference in the distribution of semantic classes between these images and may obtain a highly imbalanced response for the specific class representation in  $\mathbf{Q}$ . When aligning the image-specific semantic correlations between two cross-modal images in such a case, it may raise unstable in the training process. Here we calculate normalized summation by dividing by  $\sum_{(\frac{H}{4P}, \frac{W}{4P})} \sigma(\mathbf{S}_1^i)$  to avoid such a situation.

In our scheme, the proposed EAM outputs the above semantic correlations at Scale-1 for each modality, *i.e.* denoted by  $\mathbf{E}_{1:M_1}$  and  $\mathbf{E}_{1:M_2}$  for CT and MRI, which can be continuously updated during the training process. We advocate for dynamically aligning the semantic correlations of images from different modalities in Sec. 3.4, as we intuitively assume that the inter-class relationships shown in CT are still valid in MRI. For example, the inter-class relationship between the left kidneys and right kidneys in abdominal images should be similar.

### 3.4. Objective Functions

**Auxiliary Prediction Loss.** We introduce an auxiliary loss to supervise the semantic prediction of each pixel on multi-scale semantic-aware feature maps. Concretely, we employ convolution layer over semantic-aware feature maps at each scale to predict the segmentation labels, which is supervised by the auxiliary ground-truth at corresponding scales using cross-entropy (CE) and Dice loss (DSC).

$$\mathcal{L}_{\text{aux}} = \sum_{\lambda} \left[ \text{CE}(\mathbb{F}_{1 \times 1}(\mathbf{A}_{\lambda}), \mathbf{Y}_{\lambda}) + \text{DSC}(\mathbb{F}_{1 \times 1}(\mathbf{A}_{\lambda}), \mathbf{Y}_{\lambda}) \right], \quad (12)$$

where  $\lambda \in \{1, 2, 3\}$  represents three scales, and  $\mathbb{F}_{1 \times 1}(\cdot)$  denotes the function with a  $1 \times 1$  convolution operation to reduce the dimension of multi-head, followed by a softmax operation along class dimension.

**Modality-level Consistency Regularization.** Inspired by semantic consistency between different modalities in previous work [17, 30, 31], we introduce consistency regularization to globally align the class representations of two modalities. Let  $\mathbf{Q}_{M_1}$  and  $\mathbf{Q}_{M_2} \in \mathbb{R}^{Z \times 4C}$  denote modality-specific class embeddings of two modalities. Then the modality-level consistency regularization can be presented as follows:

$$\mathcal{L}_{\text{mcr}} = \sum_{i=1}^Z \left( 1 - \frac{\mathbf{Q}_{M_1}^i \mathbf{Q}_{M_2}^i}{\|\mathbf{Q}_{M_1}^i\| \cdot \|\mathbf{Q}_{M_2}^i\|} \right), \quad (13)$$

where  $Z$  denotes the total number of semantic classes.

**Image-level Consistency Regularization.** We further utilize the symmetrical Kullback-Leibler (KL) divergence to locally align image-specific semantic correlations of each modality. For two modalities  $M_1$  and  $M_2$ , let  $\mathbf{E}_{\lambda:M_1}^i$  and  $\mathbf{E}_{\lambda:M_2}^i$  denote correlation vectors corresponding to class  $i$ -th at Scale- $\lambda$ . The image-level consistency regularization can be presented as follows:

$$\mathcal{L}_{\text{icr}} = \sum_{\lambda} \sum_{i=1}^Z \left[ \mathcal{D}_{\text{KL}}(\sigma(\mathbf{E}_{\lambda:M_1}^i/\tau) \parallel \sigma(\mathbf{E}_{\lambda:M_2}^i/\tau)) + \mathcal{D}_{\text{KL}}(\sigma(\mathbf{E}_{\lambda:M_2}^i/\tau) \parallel \sigma(\mathbf{E}_{\lambda:M_1}^i/\tau)) \right], \quad (14)$$

where  $\mathcal{D}_{\text{KL}}(\cdot \parallel \cdot)$  denotes the relative entropy. The  $\sigma(\cdot)$  denotes the softmax operation along the class dimension.  $\tau$  is a temperature hyper-parameter to control the softness of the related probability distributions.

**Overall Objective Function.** The overall objective function of the proposed method can be presented as follows:

$$\mathcal{L} = \mathcal{L}_{\text{seg}}^{M_1} + \mathcal{L}_{\text{seg}}^{M_2} + \alpha(\mathcal{L}_{\text{aux}}^{M_1} + \mathcal{L}_{\text{aux}}^{M_2}) + \beta\mathcal{L}_{\text{mcr}} + \gamma\mathcal{L}_{\text{icr}}, \quad (15)$$

where  $\mathcal{L}_{\text{seg}}^{M_1}$  and  $\mathcal{L}_{\text{seg}}^{M_2}$  denote the segmentation losses of all training samples in modality  $M_1$  and modality  $M_2$  respectively, which are combined with their Dice losses and cross-entropy losses. Similarly, the  $\mathcal{L}_{\text{aux}}^{M_1}$  and  $\mathcal{L}_{\text{aux}}^{M_2}$  indicate auxiliary prediction losses of all training samples from two modalities. The hyper-parameters  $\alpha, \beta, \gamma$  are adopted to scale the contribution of each loss to the overall objective function. And we empirically set the  $\alpha, \beta, \gamma$  as 0.5, 0.5, and 0.5 to balance them and the main segmentation losses.

## 4. Experiments

### 4.1. Datasets and Evaluation Metrics

**Cardiac substructure segmentation.** We employ the Multi-Modality Whole Heart Segmentation Challenge 2017 dataset [35] to perform multi-class cardiac structure segmentation. The dataset is composed of unpaired 20 CT and 20 MRI scans collected from vari-

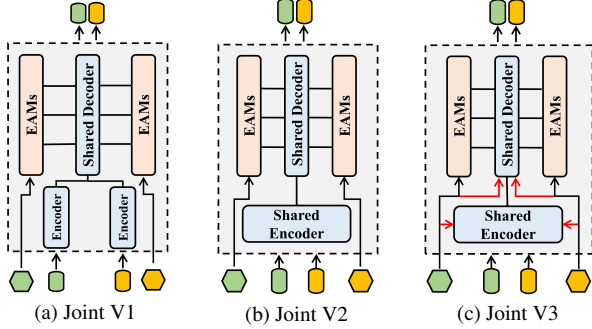


Figure 3. Three versions of Joint architecture: (a) Using modality-specific Encoder and EAMs while sharing Decoder; (b) Sharing both Encoder and Decoder while keeping EAMs as modality-specific; (c) Incorporating the modality-aware channel-wise multiplication mechanism into each transformer block of shared Encoder and Decoder in the architecture (b). Note that the input hexagons and rectangles denote modality-specific class embeddings and patch tokens, respectively.

ous patients and sites. We intend to train the segmentation network to recognize four organs for each modality: left ventricle myocardium (LVM), left atrium blood cavity (LAC), left ventricle blood cavity (LVC), and ascending aorta (AA). Since the UMMKD approach [9] achieves state-of-the-art performance, we take the same partitioning (*i.e.* training, validation and test) and pre-processing of the dataset as the UMMKD reported for a fair comparison. Specifically, we align with them to split each modality into 70% for training, 10% for validation, and 20% for testing. Before feeding into the network, we first resample both modalities to isotropic  $1\text{mm}^3$  and crop their central heart region by a 3D bounding box which has a fixed coronal plane size of  $256 \times 256$ . For each 3D cropped image, we remove the top 2% of its intensity histogram to reduce artifacts, which is then normalized to zero mean and unit variance.

**Abdominal multi-organ segmentation.** We adopt public CT data from [15] with 30 patients, and the T2-SPIR MRI data from the ISBI 2019 CHAOS Challenge [14] with 20 volumes. We focus on adapting the segmentation network to delineate four abdominal organs: liver, right kidney (R-kdy), left kidney (L-kdy), and spleen. Since the UMMKD method does not report the detailed partitioning of these two datasets, we attempt to align their practices for a more fair comparison. The UMMKD method [9], in particular, employs only 9 MRI scans from the MRI dataset and removes a low-quality CT scans from the CT dataset. As a result, we randomly select 9 MRI cases from all 20 MRI scans five times and use the entire CT images from CT dataset to demonstrate the robustness of our method, and then average the results of the five randomized experiments to compare with their method. In accordance

with UMMKD, we randomly divided each data modality into 70% for training, 10% for validation, and 20% for testing. Following UMMKD’s pre-processing methods, we first resample them into around  $1.5 \times 1.5 \times 8.0 \text{mm}^3$  with a size of  $256 \times 256$  in the coronal plane to eliminate the huge difference in voxel-spacing between two datasets, and then perform intensity normalization to zero mean and unit variance for each modality.

**Evaluation metrics.** We assess segmentation performance using the Volume Dice Coefficient (Dice, %) and Average Symmetric Surface Distance (ASD,  $mm$ ) metrics, calculating the average and standard deviation of segmentation results for each class [9]. It is worth noting that the final segmentation results (mean and standard variance) in the abdominal multi-organ segmentation task are calculated from the results of all the test samples in the five random tests.

## 4.2. Implementation Details

**2D model configuration.** For the multi-class cardiac structure segmentation, we adopt a 2D Transformer-based U-shaped Encoder-Decoder architecture named Swin-Unet [1]. The detailed network architecture is described in Table 1. We center-crop the 2D slices to generate patches of size  $224 \times 224$  as network inputs. To reduce over-fitting, we augment the data with random rotation, random width and height scaling, and horizontal/vertical flipping. During the training period, the batch size is set to 12 for each modality, and the Adam optimizer is used to optimize the network for back propagation with epsilon  $1e - 8$  and weight decay  $1e - 4$ . We set the learning rate to  $1e - 4$  and decayed using the poly strategy [29] for 100 epochs.

**3D model configuration.** For abdominal multi-organ segmentation, we employ a 3D U-shaped Transformer with volume-based self-attention mechanism and strided convolution named nnFormer [33] as the backbone. Table 1 also reports the detailed network architecture. Given the backbone’s input size requirement, we perform random crop to obtain an input with a size of  $128 \times 128 \times 64$ . We also use data enhancements such as random rotation, random scaling, random flip, and random shift intensity. For the inference, we use a sliding window with a 25% overlap to continuously crop a set of  $128 \times 128 \times 64$  patches from a test volume. The cropped patches’ segmentation predictions are stitched together to obtain the final segmentation mask based on their crop position. During the training phase, the batch size for each modality is 2. We use the Adam optimizer with epsilon  $1e - 8$  and weight decay  $1e - 4$ . The initial learning rate is set to  $1e - 4$  and gradually reduced by calculating  $(1 - \text{epoch}/\text{max\_epoch})^{0.9}$ .



Table 1. Detailed configurations of 2D Transformer and 3D Transformer architectures corresponding to Fig. 1, where  $\{G_i\}_{i=1}^4$  and  $\{L_i\}_{i=1}^4$  denote the basic number of Transformer blocks for the Encoder and Decoder respectively.

Layer	2D Transformer [1]	3D Transformer [33]
Transformer Block	Swin Transformer Block [18]	Volume-based Self-attention
Down-sampling	Patch Merging	Strided Convolution
Up-sampling	Patch Expanding	Strided Convolution
$[G_1, G_2, G_3, G_4]$	[2, 2, 2, 2]	[2, 2, 2, 2]
$[L_1, L_2, L_3, L_4]$	[2, 2, 2, 2]	[2, 2, 2, 2]
Patch Size	$4 \times 4$	$4 \times 4 \times 2$

Table 2. The performance of cardiac substructure segmentation by using 2D Transformer. The values in the bracket indicates the improvement compared with the Baseline model. The values greater than +1.5 on Dice and -0.20 on ASD are highlighted.

Methods	Cardiac CT					Cardiac MRI					Overall Mean
	LVM	LAC	LVC	AA	Mean	LVM	LAC	LVC	AA	Mean	
Dice Coefficient (avg.± std., %) ↑											
Payer <i>et al.</i>	87.2±3.9	92.4±3.6	92.4±3.3	91.1±18.4	90.8	75.2±12.1	81.1±13.8	87.7±7.7	76.6±13.8	80.2	85.5
UMMKD	88.5±3.1	91.5±3.1	93.1±2.1	93.6±4.3	91.7	80.8±3.0	86.5±6.5	93.6±1.8	83.1±5.8	86.0	88.8
Backbone	90.0±3.2	92.5±2.9	92.6±3.0	87.4±3.8	90.6	79.9±4.6	85.3±3.9	92.0±2.7	84.9±2.9	85.5	88.1
Baseline	90.6±2.8	92.6±2.8	93.2±2.5	88.9±3.4	91.3	80.9±4.0	86.3±3.8	92.9±2.3	85.8±3.5	86.5	88.9
Joint V1	89.4±2.7	93.3±3.0	92.7±2.9	92.2±2.5	91.9 (+0.6)	80.5±4.2	87.3±4.3	92.2±2.4	87.0±3.2	86.8 (+0.3)	89.3 (+0.4)
Joint V2	89.1±2.8	93.0±2.7	92.8±3.3	91.2±2.6	91.5 (+0.2)	80.2±3.9	86.5±4.5	92.0±3.0	86.1±3.8	86.2 (-0.3)	88.9 (+0.0)
Joint V3	90.0±2.3	93.8±2.1	93.4±2.4	94.0±2.0	92.8 (+1.5)	81.0±3.1	87.4±3.6	93.5±2.1	87.8±3.0	87.4 (+0.9)	90.1 (+1.2)
Joint V1+CR	90.2±2.0	93.7±1.8	93.6±2.2	95.1±1.6	93.2 (+1.9)	<b>81.8±2.7</b>	88.4±4.0	93.3±1.5	88.6±2.2	88.0 (+1.5)	90.6 (+1.7)
Joint V2+CR	90.5±2.1	93.2±2.2	93.8±2.7	94.4±1.7	93.0 (+1.7)	81.5±3.4	88.0±4.2	93.4±1.9	88.1±3.4	87.8 (+1.3)	90.4 (+1.5)
<b>Ours</b>	<b>90.9±2.0</b>	<b>94.8±1.6</b>	<b>94.5±2.1</b>	<b>95.9±1.4</b>	<b>94.0 (+2.7)</b>	81.6±2.5	<b>89.6±3.3</b>	<b>94.4±1.3</b>	<b>89.2±2.8</b>	<b>88.7 (+2.2)</b>	<b>91.4 (+2.5)</b>
Average Symmetric Surface Distance (avg.± std., mm) ↓											
Payer <i>et al.</i>	-	-	-	-	-	-	-	-	-	-	-
UMMKD	-	-	-	-	-	-	-	-	-	-	-
Backbone	1.67±0.46	1.95±0.54	1.43±0.47	1.51±0.41	1.64	2.12±1.57	1.74±0.85	1.41±0.81	3.74±1.68	2.25	1.95
Baseline	1.49±0.33	1.84±0.44	1.38±0.35	1.46±0.28	1.54	1.71±1.43	1.37±0.64	1.46±0.89	2.69±1.27	1.86	1.70
Joint V1	1.63±0.38	1.64±0.40	1.47±0.32	1.19±0.27	1.48 (-0.06)	1.99±1.07	1.36±0.57	1.51±0.73	2.89±1.33	1.94 (+0.08)	1.71 (+0.01)
Joint V2	1.58±0.35	1.70±0.44	1.39±0.35	1.33±0.38	1.50 (-0.04)	1.87±0.92	1.47±0.40	1.42±0.55	3.13±1.41	1.97 (+0.11)	1.74 (+0.04)
Joint V3	1.34±0.31	1.63±0.46	1.32±0.27	1.10±0.29	1.35 (-0.19)	1.84±0.81	1.22±0.53	1.39±0.58	2.05±1.10	1.63 (-0.23)	1.49 (-0.21)
Joint V1+CR	1.29±0.26	1.65±0.44	1.28±0.30	1.13±0.28	1.34 (-0.20)	1.76±0.87	<b>1.15±0.36</b>	1.48±0.52	<b>1.92±1.18</b>	1.58 (-0.28)	1.46 (-0.24)
Joint V2+CR	<b>1.27±0.28</b>	1.73±0.47	1.34±0.32	1.08±0.25	1.36 (-0.18)	1.69±0.85	1.18±0.47	1.50±0.64	1.97±1.26	1.59 (-0.27)	1.47 (-0.23)
<b>Ours</b>	1.31±0.27	<b>1.49±0.38</b>	<b>1.22±0.27</b>	<b>1.00±0.24</b>	<b>1.26 (-0.28)</b>	<b>1.55±0.78</b>	1.24±0.34	<b>1.27±0.32</b>	2.01±0.95	<b>1.52 (-0.34)</b>	<b>1.39 (-0.31)</b>

### 4.3. Experimental Settings

To thoroughly evaluate our method on the two multi-modality segmentation tasks, we provide three degenerate models of the proposed method. The detailed architectures are shown in Fig. 3. We take into account the eight experimental settings that conduct the fixed 2D or 3D Transformer and hyper-parameters for a fair comparison of different settings.

1) **Backbone**: training a backbone separately by using each modality.

2) **Baseline**: training a separate backbone while adding auxiliary prediction loss  $\mathcal{L}_{aux}$  for each modality.

3) **Joint V1**: training a joint Transformer with modality-specific encoder and EAMs, shared decoder, which is a conventional multi-modal learning architecture [19] as shown in Fig. 3a.

4) **Joint V2**: training a joint Transformer with shared encoder and decoder, and modality-specific EAMs, as shown in Fig. 3b.

5) **Joint V3**: Based on *Joint V2*, implementing the modality-aware channel-wise multiplication mechanism in

each transformer block of the shared encoder and decoder in accordance with Sec. 3.2, as shown in Fig. 3c.

6) **Joint V1 + CR**: training *Joint V1* Transformer with two types of consistency terms  $\mathcal{L}_{mcr}$ ,  $\mathcal{L}_{icr}$ .

7) **Joint V2 + CR**: training *Joint V2* Transformer with two types of consistency terms  $\mathcal{L}_{mcr}$ ,  $\mathcal{L}_{icr}$ .

8) **Ours (Joint V3 + CR)**: our full multi-modal learning strategy, utilizing *Joint V3* Transformer and two types of consistency terms  $\mathcal{L}_{mcr}$ ,  $\mathcal{L}_{icr}$ .

### 4.4. Effectiveness of Our Proposed framework

1) **Cardiac substructure segmentation**. We start with using the 2D Swin-Unet [1] as our *Backbone*, which has been trained with a single modal dataset. Based on this structure, we extend our *Baseline* model by introducing the auxiliary prediction loss  $\mathcal{L}_{aux}$  in Eqn.12. Table. 2 shows that *Baseline* method achieves average segmentation Dice of 91.3% on CT and 86.5% on MRI, outperforming the *Backbone* model, as well as the MICCAI-MMWHS challenge winner Payer *et al.* [20] which also deploys single modality training. This demonstrates that, similar to a form of deep supervision, calibrating multi-scale semantic-aware feature maps

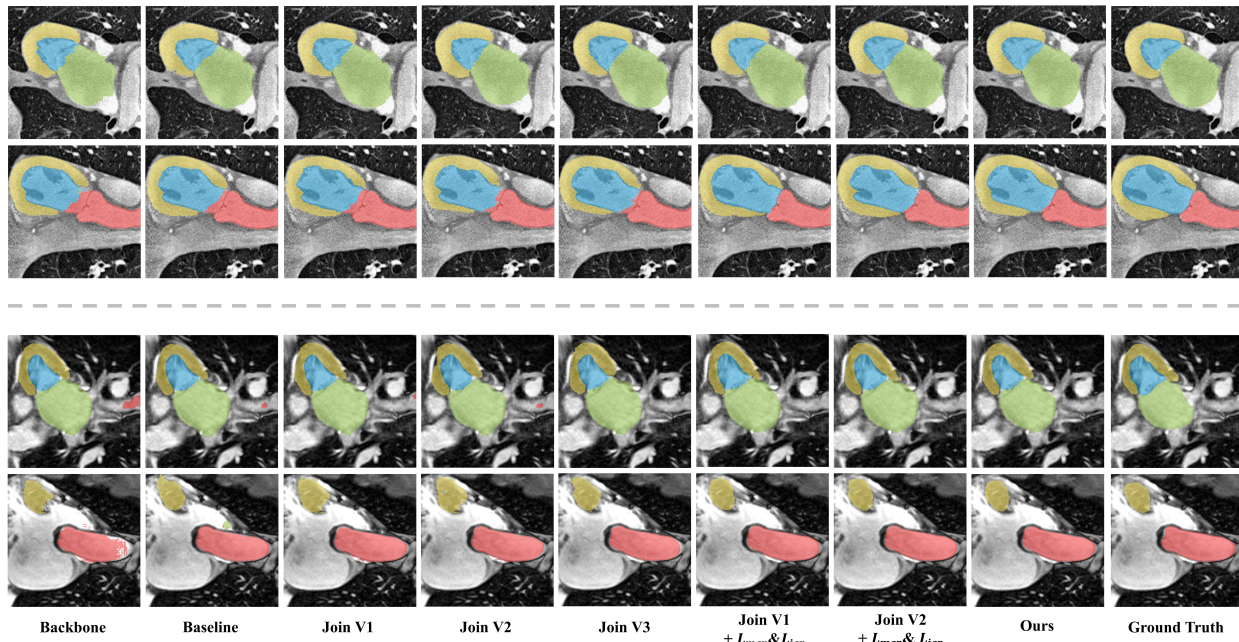


Figure 4. Visual comparison of segmentation results from different settings between MRI/CT data on cardiac segmentation task. The structures of AA, LAC, LVC and LVM are highlighted by red, green, blue, and yellow colors, respectively.

Table 3. The results of abdominal multi-organ segmentation by using 3D Transformer. The values in the bracket indicates the promotion compared with the Baseline model. The values greater than +1.5 on Dice and -0.20 on ASD are highlighted.

Methods	Abdominal CT					Abdominal MRI					Overall Mean
	Liver	Spleen	R-kdy	L-kdy	Mean	Liver	Spleen	R-kdy	L-kdy	Mean	
Dice Coefficient (avg.± std., %) ↑											
UMMKD	92.7±1.8	93.7±1.7	<b>94.0±0.7</b>	89.5±3.9	92.4	90.3±2.8	87.4±1.1	91.0±1.5	88.3±1.7	89.3	90.8
Backbone	93.2±2.8	90.9±2.4	86.9±2.7	87.5±3.8	89.5	91.7±4.0	87.2±3.2	90.9±2.7	90.6±3.3	90.1	89.9
Baseline	93.6±2.2	92.1±2.6	87.9±1.8	87.7±3.6	90.3	92.9±3.3	87.8±2.9	92.0±2.5	91.4±3.1	91.0	90.7
Joint V1	93.9±2.5	92.7±2.3	88.2±2.0	88.1±3.2	90.7 (+0.4)	93.2±2.8	88.1±2.5	92.4±2.3	91.1±3.3	91.2 (+0.2)	91.0 (+0.3)
Joint V2	94.0±2.6	92.5±2.2	87.8±2.9	87.9±3.4	90.6 (+0.3)	92.6±3.4	87.3±3.1	91.2±1.9	90.8±3.7	90.5 (-0.5)	90.5 (-0.2)
Joint V3	94.6±2.2	93.3±1.8	88.9±2.3	88.7±3.5	91.4 (+1.1)	93.8±2.3	88.5±2.7	92.7±1.5	91.5±3.1	91.6 (+0.6)	91.5 (+0.8)
Joint V1 + CR	95.3±1.8	94.3±1.1	91.6±1.0	91.2±2.5	93.1 (+2.8)	94.2±1.7	89.3±2.1	93.3±1.1	92.6±2.3	92.4 (+1.4)	92.7 (+2.0)
Joint V2 + CR	95.1±1.7	93.9±1.5	91.3±1.4	91.0±2.7	92.8 (+2.5)	94.0±1.9	89.1±1.8	92.8±0.6	92.2±2.0	92.0 (+1.0)	92.4 (+1.7)
<b>Ours</b>	<b>95.8±1.4</b>	<b>94.9±1.3</b>	92.3±0.9	<b>91.8±2.2</b>	<b>93.7 (+3.4)</b>	<b>94.7±1.5</b>	<b>89.9±1.2</b>	<b>93.6±0.8</b>	<b>93.0±1.4</b>	<b>92.8 (+1.8)</b>	<b>93.3 (+2.6)</b>
Average Symmetric Surface Distance (avg.± std., mm) ↓											
UMMKD	-	-	-	-	-	-	-	-	-	-	-
Backbone	1.19±0.91	1.18±0.82	1.84±1.06	1.10±0.78	1.33	1.20±0.68	1.27±0.79	1.36±0.94	1.37±0.71	1.30	1.31
Baseline	1.12±0.75	0.98±0.68	1.60±0.93	1.05±0.65	1.19	1.07±0.52	1.19±0.76	1.22±0.80	1.23±0.64	1.18	1.18
Joint V1	1.07±0.56	0.79±0.45	1.45±0.71	0.93±0.49	1.06 (-0.13)	1.12±0.46	1.06±0.52	1.18±0.62	1.30±0.55	1.17 (-0.01)	1.11 (-0.07)
Joint V2	1.03±0.62	0.85±0.51	1.87±0.84	0.96±0.58	1.18 (-0.01)	1.19±0.56	1.32±0.73	1.27±0.85	1.34±0.67	1.28 (+0.10)	1.23 (+0.05)
Joint V3	0.94±0.58	0.75±0.37	1.37±0.61	0.82±0.43	0.97 (-0.22)	1.01±0.49	1.18±0.64	1.03±0.69	1.15±0.53	1.09 (-0.09)	1.03 (-0.15)
Joint V1 + CR	<b>0.72±0.25</b>	0.68±0.23	0.95±0.37	<b>0.70±0.18</b>	0.76 (-0.43)	0.91±0.37	0.86±0.48	0.94±0.43	0.88±0.32	0.90 (-0.28)	0.83 (-0.35)
Joint V2 + CR	0.91±0.41	0.72±0.29	1.06±0.43	0.75±0.22	0.86 (-0.33)	0.89±0.30	0.92±0.57	0.97±0.56	0.94±0.42	0.93 (-0.25)	0.90 (-0.28)
<b>Ours</b>	0.87±0.29	<b>0.58±0.17</b>	<b>0.84±0.32</b>	0.72±0.24	<b>0.75 (-0.44)</b>	<b>0.83±0.36</b>	<b>0.56±0.23</b>	<b>0.85±0.39</b>	<b>0.83±0.37</b>	<b>0.77 (-0.41)</b>	<b>0.76 (-0.42)</b>

improves final segmentation performance noticeably.

As shown in Fig. 3a, based on the *Baseline* model, *Joint V1* exemplifies a conventional multi-modal Transformer architecture by using modality-specific encoders and EAMs while sharing decoders. This model raises the Dice value to 91.9% for CT and 86.8% for MRI. This clearly illustrates the Transformer’s ability to deal with multi-modal data with large appearance differences at the same time, as well as the potential for mutual promotion between different modalities

by sharing some modules. In Fig. 3b, *Joint V2* targets to further share decoder between different modalities to improve the parameter efficiency of multi-modal Transformer. However, there is a decrease in segmentation results, *i.e.* Dice of 91.5% on CT and 86.2% on MRI. This suggests that in such a situation, modality discrepancy has a significant impact on learned feature representations without introducing any semantic consistency constraints. In Fig. 3c, we introduce a modality-aware channel-wise multiplication mecha-

nism into each Transformer block of shared encoder and decoder. This scheme improves segmentation results to 92.8% on CT and 87.4% on MRI, demonstrating the efficiency of modality-specific activation calibration.

By leveraging proposed two types of consistency regularization terms, *i.e.*  $\mathcal{L}_{\text{mcr}}$  and  $\mathcal{L}_{\text{icr}}$ , the three multi-modal Transformer architectures *Joint V1*, *Joint V2* and *Joint V3* are all boosted. The *Joint V3* with  $\mathcal{L}_{\text{mcr}}$  and  $\mathcal{L}_{\text{icr}}$  is marked as *ours* in Table 2, and it achieves an overall Dice of 91.4% (*i.e.* the average of 94.0% on CT and 88.7% on MRI). When compared to the current state-of-the-art multi-modal approach UMMKD [9], our segmentation result has a 2.6% promotion on overall mean Dice. In addition, our method achieves the lowest overall mean ASD (*i.e.* 1.39mm) among all compared approaches. In Fig. 4, we also present a visual representation of the segmentation results of various approaches for quantitative comparison. Our segmentation result clearly shows less noise, better boundary retention, and greater precision in small areas.

**2) Abdominal multi-organ segmentation.** Here we implement the 3D nnFormer [33] as our *Backbone*. To create the *Baseline* model, we add the auxiliary prediction loss  $\mathcal{L}_{\text{aux}}$  to *Backbone*, just as we have done in the 2D case. The Dice values raise to 90.3% on CT and 91.0% on MRI, which is shown in Table 3. Likewise, the multi-modal Transformer architecture *Joint V1* improves the Dice value by 0.4% on CT and 0.2% on MRI when compared to the *Baseline* model trained from a single modality. In contrast to *Joint V1*, sharing decoder in *Joint V2* causes a slight segmentation performance drop when the number of parameters is reduced. By integrating modality-specific activation, *Joint V3* improves the Dice values to 91.4% on CT and 91.6% on MRI, outperforming both *Joint V2* and *Joint V1* by a significant margin. Furthermore, by using the  $\mathcal{L}_{\text{mcr}}$  and  $\mathcal{L}_{\text{icr}}$ , all three models improve significantly, and our full scheme achieves the best segmentation results of 93.3% overall mean Dice and 0.76mm overall mean ASD. Compared with the counterpart, the overall mean Dice values of our scheme also outperform UMMKD [9] by a large margin, *i.e.* 1.3% on CT and 3.5% on MRI. Finally, we exhibit the visual segmentation results of various approaches for quantitative comparison, as shown in Fig. 5.

**3) Few-shot segmentation.** To assess the effectiveness of our method when training with limited samples of one modality, we randomly select 1 or 3 samples from one modality’s (CT or MRI) training set while training the model with all training data from another modality. We conduct all of the few-shot segmentation experiments on MICCAI-MMWHS dataset. As shown in Table 4, when our multi-modal learning framework is trained with only 1 annotated MRI image and all CT images, the value of mean Dice for MRI is only slightly lower than *Baseline* (*i.e.* 0.4%), which is trained with all MRI images alone. This

demonstrates that when using complete CT training data, the proposed method can eliminate the impact of insufficient MRI training samples. In such a case, the mean Dice of CT improves to 92.7% and the mean ASD decreases to 1.41mm, evidencing that the feature representation of CT could also be enhanced by using only 1 MRI image. Moreover, when the number of MRI training samples increases to 3, the mean Dice values improve to 93.3% on CT and 86.9% on MRI, surpassing the *Baseline* model and UMMKD.

When training with only 1 CT image and all of MRI images using our scheme, the mean Dice of CT drops by 0.7% compared with *Baseline* model which is only trained with all of CT images. Also, giving 1 annotated CT image improves the mean Dice of MRI by 1.1% and decreases the mean ASD of MRI by 0.17mm, highlighting the mutual promotion between CT and MRI. Further, using 3 CT images raises the mean Dice to 91.5% on CT and 88.0% on MRI, defeating UMMKD by 2.0% on MRI while maintaining competitive performance on CT.

## 4.5. Ablation studies

We conduct abdominal multi-organ segmentation experiments to further investigate the effectiveness of the proposed multi-modal learning scheme, as well as the effect of hyperparameters on performance.

**1) Effectiveness of each key component.** We employ four settings to verify the contribution of various key components: (a) we train the *Joint V3* model without using any consistency regularization terms for both CT and MRI; (b) we only add the modality-level consistency regularization  $\mathcal{L}_{\text{mcr}}$  onto *Joint V3*, which corresponds to Eqn.13; (c) we only add the instance-level consistency regularization  $\mathcal{L}_{\text{icr}}$  onto *Joint V3*, which corresponds to Eqn.14; (d) we add both  $\mathcal{L}_{\text{mcr}}$  and  $\mathcal{L}_{\text{icr}}$  to accomplish our multi-modal learning scheme.

Table 5 reports the mean value of Dice and ASD for each class. Adding  $\mathcal{L}_{\text{mcr}}$  to *Joint V3* improves the average Dice to 92.9% on CT and 92.2% on MRI and decreases the average ASD to 0.83mm on CT and 0.94mm on MRI. We also observe that the segmentation performance of each class improves significantly, regardless of CT or MRI, proving that aligning the representations of each class across various modalities could narrow the modalities’ discrepancies in data distribution, allowing the network to be more generalized for both types of data. Furthermore, only adding  $\mathcal{L}_{\text{icr}}$  onto *Joint V3* results in a mean Dice improvement of 1.8% on CT and 0.7% on MRI. This demonstrates that facilitating the network to dynamically learn the consistency of inter-class relationships at the image level within different modalities could also enhance the network’s generalization to different modalities. Finally, by including both  $\mathcal{L}_{\text{mcr}}$  and  $\mathcal{L}_{\text{icr}}$ , the Dice value further improves to 93.7% on CT and 92.8% on MRI, outperforming the variants that only add



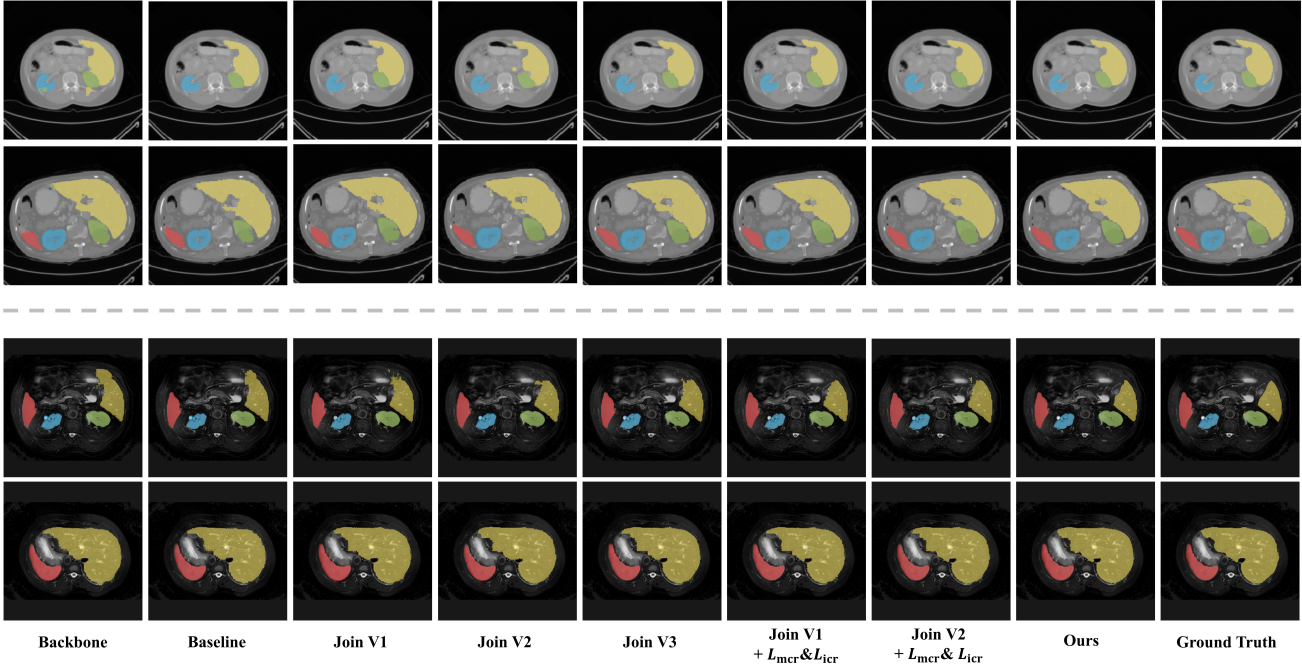


Figure 5. Visual comparison of segmentation results from different settings between MRI/CT data on abdominal multi-organ segmentation task. The structures of spleen, R-kdy, L-kdy and Liver are highlighted by red, green, blue and yellow colors, respectively.

$\mathcal{L}_{mcr}$  and  $\mathcal{L}_{icer}$ , verifying that the two regularization terms can be used jointly to pursue the structured semantic consistency and effectively improve the segmentation performance.

2) *Setting of temperature hyperparameters.* The hyperparameter  $\tau$  in  $\mathcal{L}_{icer}$  is used to control the softness of the inter-class probability distributions. We vary the value of  $\tau$  to see how it affects the final segmentation results. As  $\tau$  only influences the  $\mathcal{L}_{icer}$ , we implement the *Joint V3* model with only  $\mathcal{L}_{icer}$  added. Fig. 6 presents the segmentation performance changes (*i.e.* overall mean Dice). As the temperature  $\tau$  increases from 1 to 4, the inter-class relation retains richer semantic information to guide the cross-modality learning. However, when  $\tau > 4$ , the more difficult pixel-wise constraints are exploited, and segmentation performance begins to deteriorate, possibly due to optimization difficulties. Based on the above results, we use  $\tau = 4$  in all subsequent experiments.

## 5. Discussion

This paper aims to address cross-modal medical image segmentation based on the unpaired training samples, *e.g.*, CT and MRI images. Such multi-modal learning allows a single model to analyze data from multiple imaging devices, which greatly improves the efficiency of data usage. Specifically, we can leverage cross-modal information to make better use of the limited annotated samples and achieve mu-

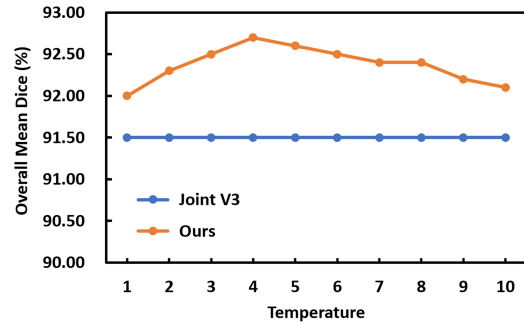


Figure 6. The effect of temperature  $\tau$ . Joint V3 is only used for comparison.

tual promotion of the performance of each modality. In practice, the main difficulty is caused by the distinct physical principles of the underlying image acquisition, leading to the large visual variance of multi-modal images. There exists limited studies to address such an open issue. In the literature, Dou *et al.* [9] proposed a pioneer work to reuse most of network parameters, by sharing all convolutional kernels across different modalities, and conduct specific modality predictions by switching modality-specific internal normalization layers. This approach is more about learning to store idiosyncratic information of certain modalities in the corresponding normalization layers, rather than embedding semantic associations between modalities into the network parameters through model training. Moreover,



Table 4. The results of **few-shot** cardiac segmentation by using 2D network. The values in the bracket indicate the promotion compared with the Baseline model. The values greater than **+1.5** on Dice and **-0.20** on ASD are highlighted.

Methods	Cardiac CT					Cardiac MRI					Overall Mean
	LVM	LAC	LVC	AA	Mean	LVM	LAC	LVC	AA	Mean	
Dice Coefficient (avg.± std., %) ↑											
Baseline	90.6±2.8	92.6±2.8	93.2±2.5	88.9±3.4	91.3	80.9±4.0	86.3±3.8	92.9±2.3	85.8±3.5	86.5	88.9
Ours	90.9±2.0	94.8±1.6	94.5±2.1	95.9±1.4	94.0	81.6±2.5	89.6±3.3	94.4±1.3	89.2±2.8	88.7	91.4
One annotated MRI	90.7±2.7	93.1±2.5	93.3±2.8	93.7±2.4	92.7 (+1.4)	78.8±5.8	85.2±4.6	92.5±3.2	87.9±4.1	86.1 (-0.4)	89.4 (+0.5)
Three annotated MRI	90.4±2.3	93.7±2.0	93.9±2.7	95.0±1.9	93.3 (+1.2)	80.6±4.7	86.0±4.1	92.6±2.9	88.2±3.3	86.9 (+0.4)	90.1 (+1.4)
One annotated CT	88.2±3.4	91.2±3.5	91.4±2.2	91.6±3.3	90.6 (-0.7)	80.8±4.2	87.9±4.3	93.1±2.1	88.6±2.9	87.6 (+1.1)	89.1 (+0.2)
Three annotated CT	88.9±3.1	91.7±2.9	92.4±2.3	92.8±2.8	91.5 (+0.2)	81.1±3.7	88.4±3.5	93.5±1.8	88.9±2.7	88.0 ( <b>+1.5</b> )	89.7 (+0.8)
Average Symmetric Surface Distance (avg.± std., mm) ↓											
Baseline	1.49±0.33	1.84±0.44	1.38±0.35	1.46±0.28	1.54	1.71±1.43	1.37±0.64	1.46±0.89	2.69±1.27	1.86	1.70
Ours	1.31±0.27	1.49±0.38	1.22±0.27	1.00±0.24	1.26	1.55±0.78	1.24±0.34	1.27±0.32	2.01±0.95	1.52	1.39
One annotated MRI	1.34±0.34	1.68±0.48	1.37±0.36	1.25±0.30	1.41 (-0.13)	1.89±1.59	2.04±0.93	1.63±1.01	2.36±1.18	1.98 (+0.12)	1.70 (+0.00)
Three annotated MRI	1.41±0.37	1.55±0.41	1.34±0.47	1.16±0.26	1.37 (-0.17)	1.73±1.28	1.82±0.87	1.51±0.83	2.24±1.06	1.83 (-0.04)	1.60 (-1.00)
One annotated CT	1.86±0.58	2.13±0.86	1.92±0.92	1.31±0.35	1.81 (+0.27)	1.75±1.31	1.44±0.47	1.42±0.75	2.08±1.02	1.67 (-0.19)	1.74 (+0.04)
Three annotated CT	1.69±0.44	1.95±0.71	1.61±0.59	1.26±0.37	1.63 (+0.09)	1.62±0.94	1.34±0.52	1.36±0.49	2.14±1.12	1.62 ( <b>-0.24</b> )	1.62 (-0.08)

Table 5. Ablation studies on abdominal multi-organ segmentation with 3D Transformer. In the brackets are the gaps to the Joint V3 counterpart. The improvements greater than **+1.5** on Dice and **-0.20** on ASD are highlighted by **green**.

Methods	Abdominal CT					Abdominal MRI					Overall Mean
	Liver	Spleen	R-kdy	L-kdy	Mean	Liver	Spleen	R-kdy	L-kdy	Mean	
Dice Coefficient (avg.± std., %) ↑											
Joint V3	94.6±2.2	93.3±1.8	88.9±2.3	88.7±3.5	91.4	93.8±2.3	88.5±2.7	92.7±1.5	91.5±3.1	91.6	91.5
Joint V3 + $\mathcal{L}_{mcr}$	95.3±2.0	94.4±1.9	91.1±1.5	90.8±3.1	92.9 ( <b>+1.5</b> )	94.2±1.8	89.0±1.7	93.3±1.2	92.1±1.9	92.2 (+0.6)	92.5 (+1.0)
Joint V3 + $\mathcal{L}_{icr}$	95.1±1.8	94.5±1.6	91.6±1.7	91.6±2.8	93.2 ( <b>+1.8</b> )	94.4±1.6	89.3±1.5	93.0±1.6	92.4±2.2	92.3 (+0.7)	92.7 (+1.2)
Joint V3 + $\mathcal{L}_{mcr}$ + $\mathcal{L}_{icr}$	95.8±1.4	94.9±1.3	92.3±0.9	91.8±2.2	93.7 ( <b>+2.3</b> )	94.7±1.5	89.9±1.2	93.6±0.8	93.0±1.4	92.8 (+1.2)	93.3 ( <b>+1.8</b> )
Average Symmetric Surface Distance (avg.± std., mm) ↓											
Joint V3	0.94±0.58	0.75±0.37	1.37±0.61	0.82±0.43	0.97	1.01±0.49	1.18±0.64	1.03±0.69	1.15±0.53	1.09	1.03
Joint V3 + $\mathcal{L}_{mcr}$	0.91±0.46	0.67±0.31	0.98±0.52	0.77±0.37	0.83 (-0.14)	0.96±0.43	0.79±0.45	0.98±0.66	1.04±0.49	0.94 (-0.15)	0.89 (-0.14)
Joint V3 + $\mathcal{L}_{icr}$	0.88±0.37	0.65±0.28	0.93±0.43	0.74±0.33	0.80 (-0.17)	0.91±0.35	0.74±0.38	0.89±0.51	0.96±0.45	0.88 ( <b>-0.21</b> )	0.84 (-0.19)
Joint V3 + $\mathcal{L}_{mcr}$ + $\mathcal{L}_{icr}$	0.87±0.29	0.58±0.17	0.84±0.32	0.72±0.24	0.75 ( <b>-0.22</b> )	0.83±0.36	0.56±0.23	0.85±0.39	0.83±0.37	0.77 ( <b>-0.32</b> )	0.76 (-0.27)

such a method requires maintaining different normalization layers for different modalities, which is unfriendly during the deployment of the model, especially for embedded intelligent devices.

To better exploit the cross-modality information, we propose a novel method to accomplish cross-modal segmentation through learning structured semantic consistency between different modalities. Our model is designed for unpaired multi-modal images and is stable during the training phase. To learn structured semantic consistency across modalities (*i.e. the consistencies of semantic class representations and their correlations.*), we introduce a carefully designed External Attention Module (EAM) to conduct semantic consistency regularizations both at the modality and image levels. Such a module is very simple and flexible to use. It is only an external module used to embed cross-modal semantic consistency into the backbone network during the training phase, thus can be removed during the testing phase, ensuring the simplicity of the model. Moreover, the input of EAM is only the feature maps extracted at the specific scale. Therefore, it can be easily integrated onto various existing 2D and 3D Transformer architectures.

During the training process, we first construct globally learnable class embeddings for each modality, with the goal of capturing the representation of each class within each modality. Given that we use the same label taxonomy for unpaired CT and MRI, one intuitive strategy for learning

consistent semantic information is to directly align class representations across modalities. However, we find that globally aligned class representations will not render the network more robust to sample variations. Driven by such a discovery, we further encourage the network to learn consistent semantic information at the image-level. The previous approach [9] directly align confusion matrices of predicted results across modalities. In contrast, we highlight semantic propagation at multiple scales from global to local, by interacting the global class representations across the entire dataset with the semantic features of each image, so as to learn image-specific class representations. Then, we derive multi-scale inter-class correlations within each image and dynamically establish its consistency between different modal data during training.

We conduct extensive evaluations on two medical image segmentation scenarios, outperforming the state-of-the-art methods with a large margin, *i.e.* 3.3% and 2.5% improvements on overall mean Dice for two tasks respectively. We further utilize few-shot setting to see how our method performs when one modality has far fewer samples than the other. Surprisingly, we find that a modality with a small number of training samples can boost the training of another modality with a large number of training samples, and a modality with a large number of training samples can greatly supplement the problem of another modality with a small number of training samples. And it is worth noting

that since Transformer requires a large amount of data for training, we still initialize the model pretrained on ImageNet [7] for both datasets due to the limited data availability, otherwise, the performance will suffer. We will continue to train on large-scale medical datasets in the future to validate our methods, such as MICCAI AMOS 2022 [12].

A few limitations of the proposed method should be mentioned. Although the proposed method outperforms the state-of-the-art unpaired multi-modal learning schemes, the segmentation accuracy still has very huge room for improvement since we only use the basic Transformer architectures. This should be acceptable since we mainly focus on learning to align the structured semantic information from different modalities but not the detailed backbone network architecture design for pixel-level predictions. In addition, although the proposed method allows exploring more modalities (*e.g.*, CT, MRI, and X-ray) to learn semantic consistencies simultaneously. When the number of modalities increases, how to align the semantic consistencies across these modalities is still not well addressed. One of the most straightforward ways is to group all modalities in pairs and align them one group by another. However, such a scheme may not be the most efficient one when training the model. We plan to design a simple yet effective strategy to tackle the above issue in our future work.

Overall, we propose a novel scheme to learn structured semantic consistency between different modalities from unpaired samples via an attention mechanism. We apply it to the joint semantic segmentation of CT and MRI, whose appearances have a large discrepancy, and it achieves significant progress compared with counterparts. Intuitively, such a scheme can be easily extended to other domain alignment problems. For example, it can also learn unified abdominal organ representations from multiple datasets with different label taxonomy. This is common in practice, *e.g.*, some datasets label the `left kidney` and `right kidneys` as the same kind, while others label them as different semantic classes, or some datasets label the `intestines` as a single class, while others distinguish it with different segments. To tackle such an issue, we just need to introduce a learnable transformation matrix in our proposed EAM module to learn the mapping relationships between different semantic labels. We will explore these extensions in future work.

## 6. Conclusion

In this paper, we study how to train the single segmentation model to conduct multi-modal medical image predictions. A novel Transformer-based framework is introduced to tackle such a problem, which adopts the modality-specific class embeddings and a newly designed plug-and-play External Attention Module (EAM) to pursue the structured semantic consistency, *i.e.* modality-specific class rep-

resentations and image-specific inter-class correlations. In the test phase, all of the modules used for modality alignment can be removed, guaranteeing ease of use in practice. Extensive experimental results demonstrate the effectiveness of the proposed method, especially by using limited training samples for the specific modality. The future work may focus on large-scale multi-modal medical data pre-training and structured knowledge discovery by adopting the proposed framework.

## References

- [1] Hu Cao et al. Swin-unet: Unet-like pure transformer for medical image segmentation. *arXiv preprint arXiv:2105.05537*, 2021. 1, 3, 5, 8, 9
- [2] Xiaohuan Cao, Jianhua Yang, Yaozong Gao, Yanrong Guo, Guorong Wu, and Dinggang Shen. Dual-core steered non-rigid registration for multi-modal images via bi-directional image synthesis. *Medical image analysis*, 41:18–31, 2017. 1
- [3] Cheng Chen, Qi Dou, Hao Chen, Jing Qin, and Pheng Ann Heng. Unsupervised bidirectional cross-modality adaptation via deeply synergistic image and feature alignment for medical image segmentation. *IEEE transactions on medical imaging*, 39(7):2494–2505, 2020. 1, 2
- [4] Chun-Fu Chen, Quanfu Fan, and Rameswar Panda. Crossvit: Cross-attention multi-scale vision transformer for image classification. *arXiv preprint arXiv:2103.14899*, 2021. 3
- [5] Jieneng Chen et al. Transunet: Transformers make strong encoders for medical image segmentation. *arXiv preprint arXiv:2102.04306*, 2021. 3
- [6] Jianhong Cheng, Jin Liu, Hulin Kuang, and Jianxin Wang. A fully automated multimodal mri-based multi-task learning for glioma segmentation and idh genotyping. *IEEE Transactions on Medical Imaging*, 2022. 1
- [7] Jia Deng, Wei Dong, Richard Socher, Li-Jia Li, Kai Li, and Li Fei-Fei. Imagenet: A large-scale hierarchical image database. In *2009 IEEE conference on computer vision and pattern recognition*, pages 248–255. Ieee, 2009. 14
- [8] Alexey Dosovitskiy et al. An image is worth 16x16 words: Transformers for image recognition at scale. *arXiv preprint arXiv:2010.11929*, 2020. 2
- [9] Qi Dou, Quande Liu, Pheng Ann Heng, and Ben Glocker. Unpaired multi-modal segmentation via knowledge distillation. *IEEE transactions on medical imaging*, 39(7):2415–2425, 2020. 1, 2, 8, 11, 12, 13
- [10] Yunhe Gao, Mu Zhou, and Dimitris N Metaxas. Utinet: a hybrid transformer architecture for medical image segmentation. In *International Conference on Medical Image Computing and Computer-Assisted Intervention*, pages 61–71, 2021. 1
- [11] Yuankai Huo et al. Synseg-net: Synthetic segmentation without target modality ground truth. *IEEE transactions on medical imaging*, 38(4):1016–1025, 2018. 2
- [12] Yuanfeng Ji et al. Multi-modality abdominal multi-organ segmentation challenge 2022. <https://amos22.grand-challenge.org/>. 2022. 14

- [13] Rashed Karim et al. Algorithms for left atrial wall segmentation and thickness–evaluation on an open-source ct and mri image database. *Medical image analysis*, 50:36–53, 2018. [1](#)
- [14] A Emre Kavur et al. Chaos challenge-combined (ct-mr) healthy abdominal organ segmentation. *Medical Image Analysis*, 69:101950, 2021. [8](#)
- [15] B Landman, Z Xu, J Igelsias, M Styner, T Langerak, and A Klein. 2015 miccai multi-atlas labeling beyond the cranial vault workshop and challenge. 2015. [8](#)
- [16] Xiaomeng Li et al. 3d multi-scale fcn with random modality voxel dropout learning for intervertebral disc localization and segmentation from multi-modality mr images. *Medical image analysis*, 45:41–54, 2018. [1](#)
- [17] Quande Liu, Lequan Yu, Luyang Luo, Qi Dou, and Pheng Ann Heng. Semi-supervised medical image classification with relation-driven self-ensembling model. *IEEE transactions on medical imaging*, 39(11):3429–3440, 2020. [7](#)
- [18] Ze Liu et al. Swin transformer: Hierarchical vision transformer using shifted windows. *arXiv preprint arXiv:2103.14030*, 2021. [3](#), [9](#)
- [19] Dong Nie, Li Wang, Yaozong Gao, and Dinggang Shen. Fully convolutional networks for multi-modality isointense infant brain image segmentation. In *2016 IEEE 13th international symposium on biomedical imaging (ISBI)*, pages 1342–1345. IEEE, 2016. [9](#)
- [20] Christian Payer, Darko Štern, Horst Bischof, and Martin Urschler. Multi-label whole heart segmentation using cnns and anatomical label configurations. In *International Workshop on Statistical Atlases and Computational Models of the Heart*, pages 190–198, 2017. [9](#)
- [21] Yongming Rao, Wenliang Zhao, Benlin Liu, Jiwen Lu, Jie Zhou, and Cho-Jui Hsieh. Dynamicvit: Efficient vision transformers with dynamic token sparsification. *arXiv preprint arXiv:2106.02034*, 2021. [3](#)
- [22] Hugo Touvron, Matthieu Cord, Matthijs Douze, Francisco Massa, Alexandre Sablayrolles, and Hervé Jégou. Training data-efficient image transformers & distillation through attention. In *International Conference on Machine Learning*, pages 10347–10357. PMLR, 2021. [3](#)
- [23] Hugo Touvron, Matthieu Cord, Alexandre Sablayrolles, Gabriel Synnaeve, and Hervé Jégou. Going deeper with image transformers. In *Proceedings of the IEEE/CVF International Conference on Computer Vision*, pages 32–42, 2021. [4](#)
- [24] Jeya Maria Jose Valanarasu, Poojan Oza, Ilker Hacihaliloglu, and Vishal M Patel. Medical transformer: Gated axial-attention for medical image segmentation. In *International Conference on Medical Image Computing and Computer-Assisted Intervention*, pages 36–46, 2021. [1](#)
- [25] Vanya V Valindria et al. Multi-modal learning from unpaired images: Application to multi-organ segmentation in ct and mri. In *2018 IEEE winter conference on applications of computer vision (WACV)*, pages 547–556, 2018. [1](#), [2](#)
- [26] Ashish Vaswani et al. Attention is all you need. In *Advances in neural information processing systems*, pages 5998–6008, 2017. [4](#)
- [27] Wenxuan Wang, Chen Chen, Meng Ding, Hong Yu, Sen Zha, and Jiangyun Li. Transbts: Multimodal brain tumor segmentation using transformer. In *International Conference on Medical Image Computing and Computer-Assisted Intervention*, pages 109–119, 2021. [1](#)
- [28] Wenhai Wang et al. Pyramid vision transformer: A versatile backbone for dense prediction without convolutions. *arXiv preprint arXiv:2102.12122*, 2021. [3](#)
- [29] Changqian Yu, Jingbo Wang, Chao Peng, Changxin Gao, Gang Yu, and Nong Sang. Bisenet: Bilateral segmentation network for real-time semantic segmentation. In *Proceedings of the European conference on computer vision (ECCV)*, pages 325–341, 2018. [8](#)
- [30] Wenguang Yuan, Jia Wei, Jiabing Wang, Qianli Ma, and Tolga Tasdizen. Unified attentional generative adversarial network for brain tumor segmentation from multimodal unpaired images. In *International Conference on Medical Image Computing and Computer-Assisted Intervention*, pages 229–237, 2019. [7](#)
- [31] Zizhao Zhang, Lin Yang, and Yefeng Zheng. Translating and segmenting multimodal medical volumes with cycle-and shape-consistency generative adversarial network. In *Proceedings of the IEEE conference on computer vision and pattern Recognition*, pages 9242–9251, 2018. [7](#)
- [32] Sixiao Zheng et al. Rethinking semantic segmentation from a sequence-to-sequence perspective with transformers. In *Proceedings of the IEEE/CVF Conference on Computer Vision and Pattern Recognition*, pages 6881–6890, 2021. [3](#)
- [33] Hong-Yu Zhou, Jiansen Guo, Yinghao Zhang, Lequan Yu, Liansheng Wang, and Yizhou Yu. nnformer: Interleaved transformer for volumetric segmentation. *arXiv preprint arXiv:2109.03201*, 2021. [1](#), [3](#), [5](#), [8](#), [9](#), [11](#)
- [34] Lei Zhu, Kaiyuan Yang, Meihui Zhang, Ling Ling Chan, Teck Khim Ng, and Beng Chin Ooi. Semi-supervised unpaired multi-modal learning for label-efficient medical image segmentation. In *International Conference on Medical Image Computing and Computer-Assisted Intervention*, pages 394–404, 2021. [2](#)
- [35] Xiahai Zhuang et al. Evaluation of algorithms for multi-modality whole heart segmentation: an open-access grand challenge. *Medical image analysis*, 58:101537, 2019. [7](#)